

# Extracting Images and Displacements from Raw Spectral Domain Optical Coherence Tomography Data

Jaeho Cho

*ECE444 - Bioinstrumentation and Sensing*  
*The Cooper Union for the Advancement of Science and Art*  
 New York City, NY  
 jaeho.cho@cooper.edu

**Abstract**—Lorem ipsum dolor sit amet, consectetur adipiscing elit, sed do eiusmod tempor incididunt ut labore et dolore magnam aliquam quaerat voluptatem. Ut enim aequale doleamus animo, cum corpore dolemus, fieri tamen permagna accessio potest, si aliquod aeternum et infinitum impendere.

**Index Terms**—SD-OCT, SDPM, Medical Imaging

## I. INTRODUCTION

Optical coherence tomography (OCT) is an optical imaging modality that can perform high resolution, cross-sectional imaging by measuring echoes of backscattered light. The unique features of OCT make it a powerful imaging modality for many fundamental research and clinical applications.

OCT performs internal imaging by measuring the magnitude and echo time delay of backscattered light. Cross-sectional images are generated by performing multiple axial measurements of echo time delay (A-scans) and scanning the incident optical beam transversely. This produces a two-dimensional data set, which represents the optical backscattering in a cross-sectional plane through the sample (B-scan).

Repeated A-scans at the same location as a function of time can be used to generate a time-resolved image (M-scan). This technique called Spectral domain phase microscopy (SDPM) is useful for measuring the displacement of structures within the sample.

Spectral domain optical coherence tomography (SD-OCT) is a type of OCT that uses a spectrometer to capture the interference pattern of light reflected from a sample and a reference arm. In SD-OCT, the source is broadband and continuous-wave, the reference arm length is fixed at a position approximately corresponding to the position of the sample, and the spectral interference pattern between the light returning from the reference arm and all depths in the sample is dispersed by a spectrometer and collected simultaneously on an array detector such as a photodiode array or charge-coupled device (CCD). The spectral information is then used to reconstruct depth-resolved images of the sample.

The detector current ( $I_D$ ) can be expressed as a function of wavenumber ( $k$ ), commonly known as the “spectral interferogram”:

$$I_D(k) = \frac{\rho}{4} [S(k)(R_R + R_{S1} + R_{S2} + \dots)] + \frac{\rho}{2} \left[ S(k) \sum_{n=1}^N \sqrt{R_R R_{S_n}} \cos(2k(z_R - z_{S_n})) \right] + \frac{\rho}{4} \left[ S(k) \sum_{n \neq m=1}^N \sqrt{R_{S_n} R_{S_m}} \cos(2k(z_{S_n} - z_{S_m})) \right] \quad (1)$$

where  $\rho$  is the responsivity of the detector,  $S(k)$  is the spectral dependence of the light source,  $R_R$  is the power reflectivity of the reference reflector,  $R_{\{S_n\}}$  is the power reflectivity of the sample reflector, and  $z_R$  and  $z_{\{S_n\}}$  are the pathlength variables in the reference and sample arms measured from the beamsplitters, respectively. The first component is the “DC Terms”, the second is the “Cross-correlation Terms” and the third is the “Auto-correlation Terms” [1].

The internal reflectivity profile of the sample can be estimated from the inverse Fourier transform of  $I_D(k)$ , generating an A-scan expressed as:

$$i_D(z) = \frac{\rho}{8} [\gamma(z)[R_R + R_{S1} + R_{S2} + \dots]] + \frac{\rho}{4} \sum_{n=1}^N \sqrt{R_R R_{S_n}} [\gamma[2(z_R - z_{S_n})] + \gamma[-2(z_R - z_{S_n})]] + \frac{\rho}{8} \sum_{n \neq m=1}^N \sqrt{R_{S_n} R_{S_m}} [\gamma[2(z_{S_n} - z_{S_m})] + \gamma[-2(z_{S_n} - z_{S_m})]] \quad (2)$$

where  $\gamma(z)$  is inverse Fourier transform of the source spectrum [1].

## II. METHODOLOGY

### A. Data Acquisition

The raw data were acquired in air, which has of an index of refraction ( $n$ ) of 1, using a ThorLabs Telesto 3, which uses an SLD with a center wavelength ( $\lambda_0$ ) of 1310 nm, bandwidth ( $\Delta\lambda$ ) of 100 nm; and an LSM-03 objective lens with numerical aperture (NA) of 0.055. Raw OCT data were collected in the form of A-scans, with each A-scan containing 2048 pixels each representing a depth of 3.6  $\mu\text{m}$ .

Assuming that the lateral resolution is limited by the con-focal geometrical optics, and the axial resolution is limited by

the low-coherence interferometer; the lateral resolution ( $\delta x$ ) can be calculated as,

$$\delta x = 0.37 \frac{\lambda_0}{\text{NA}} \approx 8.81 \mu\text{m} \quad (3)$$

and the axial resolution ( $\delta z$ ),

$$\delta z = l_c = \frac{2 \ln(2)}{\pi} \frac{\lambda_0^2}{\Delta \lambda} \approx 7.57 \mu\text{m} \quad (4)$$

where  $l_c$  is the coherence length [1].

To improve the signal-to-noise ratio (SNR) and reduce artifacts, background scans were collected along with the sample scans to perform background subtraction.

As the sample was kept entirely to one side of the zero path length, the mirror image artifacts can be simply removed by displaying only the positive distances [1]. This correction results in the pixel aspect ratio of the Bscans to be double that of images without accounting for the mirror image artifacts; approximately 0.271 instead of 0.136.

### B. Image Processing

All processing and analysis were performed using MATLAB.

a) *A-scan*: The raw data is initially captured as interferometric measurements given by the detector current. To reconstruct the internal sample reflectivity profile, the detector current first needs to be transformed from their original wavelength-based form into a uniformly spaced wavenumber (k-space) domain, which can be accomplished by a matrix multiplication. As can be seen in Fig. 1, the transformation to the k-domain does not significantly change the actual signal. Next, the signal undergoes background subtraction, where the average of the background scans is subtracted from the sample scan. This step is effective for removing the DC component in equation (1). As Fig. 1 shows, the background subtracted signal has noticeably more high frequency fluctuations. Fig. 2 also shows the difference between the raw detector currents of the sample and background scans. As the signal needs to be transformed into the spatial domain, a windowing function is applied to minimize spectral leakage and reduce artifacts. The windowing function is applied in the k-space domain, and the resulting signal is then deconvolved to compensate for system-induced distortions, which can further enhance resolution and image quality. Finally, a Fourier transform is performed to convert the signal from the k-space domain into spatial coordinates, yielding the depth-resolved reflectivity profile.

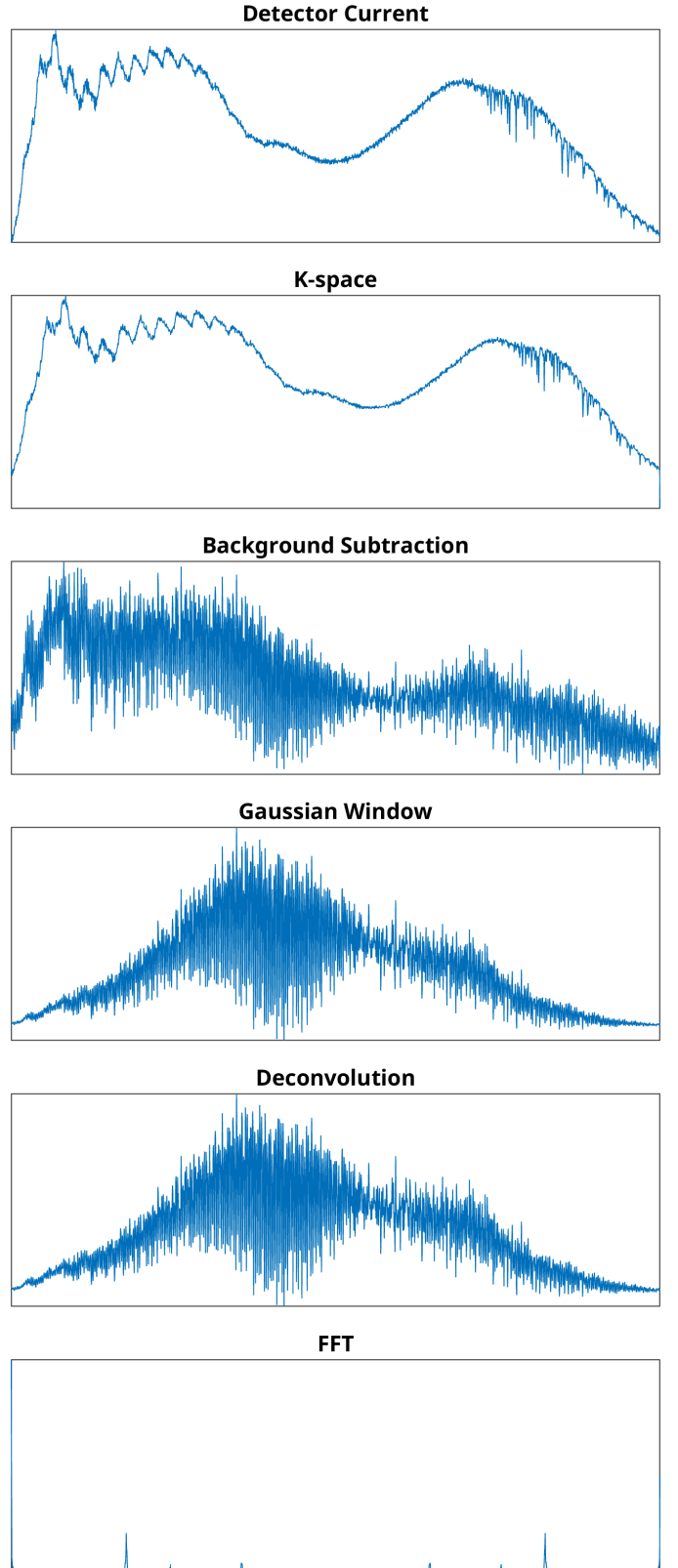


Fig. 1: Generation of an A-scan from Detector Current to reflectivity. The raw data is transformed from wavelength to wavenumber, followed by background subtraction, windowing, and deconvolution. The final step involves a Fourier transform to obtain the depth-resolved reflectivity profile.

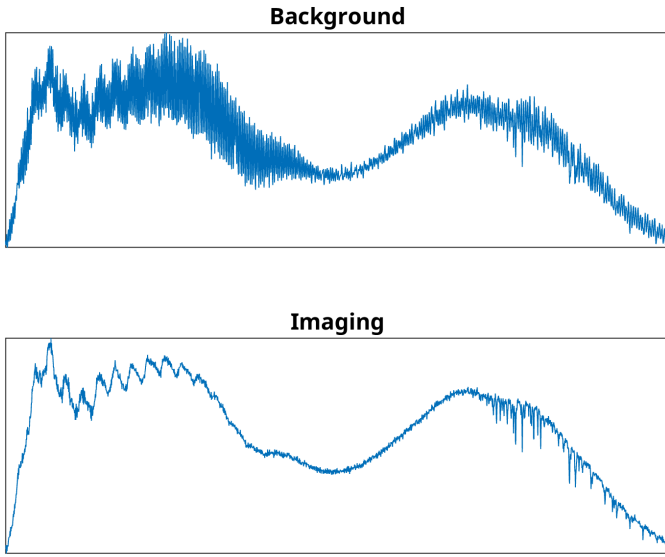


Fig. 2: Comparison of raw detector currents from the sample and background scans.

b) *B-scan*: The B-scan data consisted of 10,000 A-scans of the sample, and 175 backgrounds. The B-scan image was generated by stacking the A-scans together, and cropping to account for the mirror image artifact. The B-scan was then processed to improve the image quality by simply clipping the range of pixel values to around the max and minimum magnitudes of the region of interest illustrated in Fig. 3.

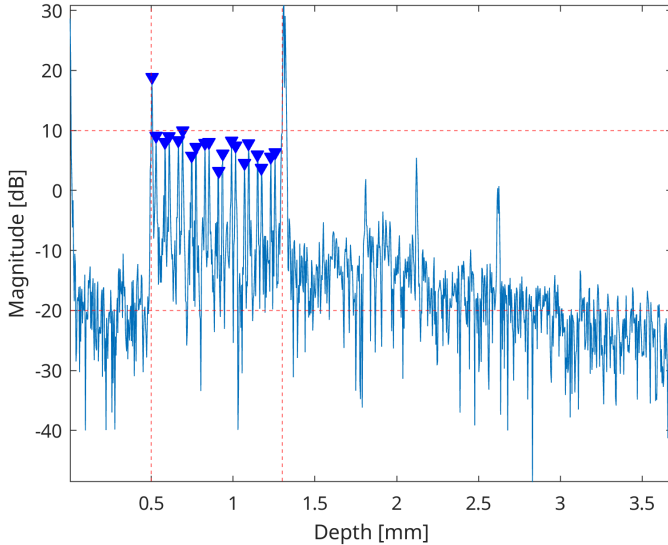


Fig. 3: A-scan at the center of the B-scan data, with the thresholds for the region of interest marked. The peaks within the region of interest are marked and were used to mark the edges of the tape layers.

Using the A-scan given in Fig. 3, the thickness of the tape layers were measured as the difference between the pairs of peaks and averaged. It was assumed that the larger difference between pairs of peaks corresponded to the tape layers, and the smaller difference corresponded to the distance between the tape layers.

c) *Mscan*:

### III. RESULTS

The generation of the A-scans is shown in Fig. 4 and the time of each processing step during each generation is given in Table I. Furthermore, the effect of deconvolution and background subtraction on the A-scan generation is shown in Fig. 5.

TABLE I: PROCESSING TIMES

Process	L2K	BGS	Window	Deconv	FFT
B-scan	0.1877	0.0127	0.0144	0.0143	0.0215
B-scan Deconv	0.1882	0.0129	0.0132	NA	0.0219
B-scan BGS Deconv	0.2095	NA	0.0132	NA	0.0221
M-scan1	1.8668	0.1335	0.1335	0.1373	0.2261
M-scan40	1.9084	0.1360	0.1362	0.1361	0.2303

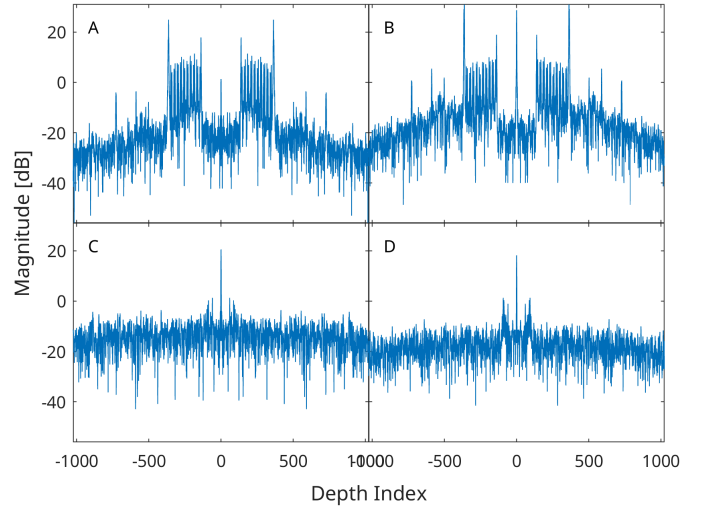


Fig. 4: A-scans of the raw data. A) the first A-scan of the Bscan data B) A-scan at the center of the Bscan data C) A-scan at the center of the Mscan1 data D) A-scan at the center of the Mscan40 data

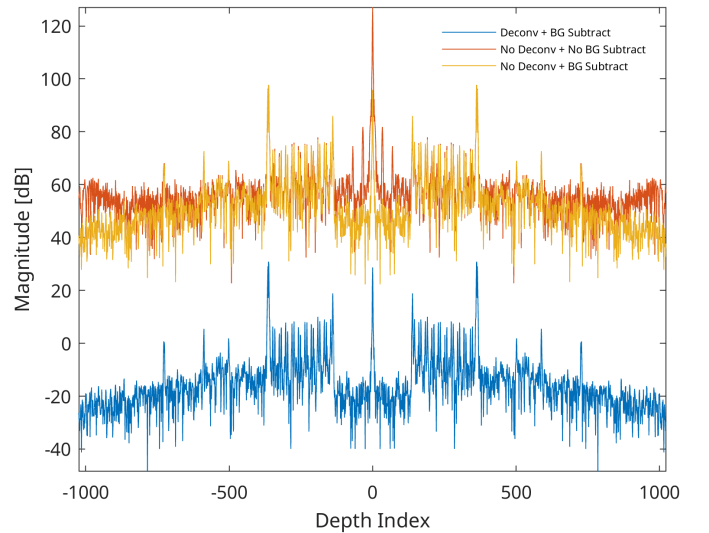


Fig. 5: Comparison of A-scan generation with and without deconvolution or background subtraction

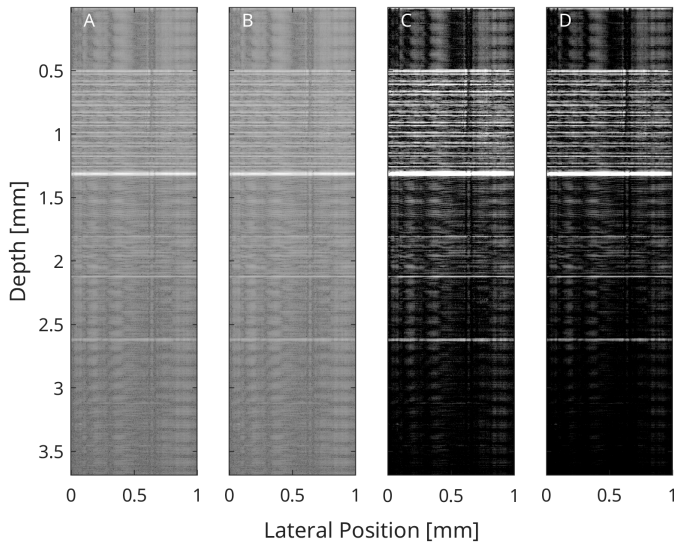


Fig. 6: A) Unprocessed B-scan B) unprocessed B-scan without deconvolution C) processed B-scan D) processed B-scan without deconvolution

A close up of the layers of tape is shown in Fig. 7 and 10 layers of tape are counted. From the analysis of Fig. 3, the thickness of the tape layers were on average 0.0552 mm; and the distance between the layers was 0.0256 mm.

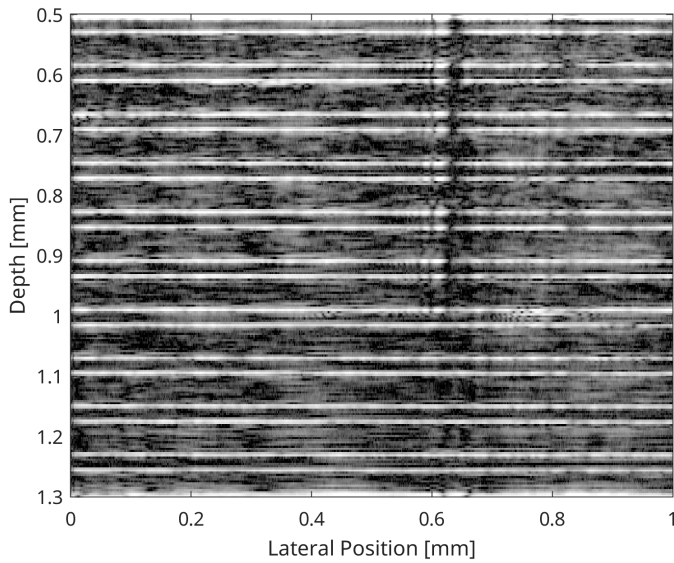


Fig. 7: A magnified view of the tape layers from the processed B-scan image. The large gaps are interpreted as the tape layers, and the smaller gaps are interpreted as the distance between the tape layers.

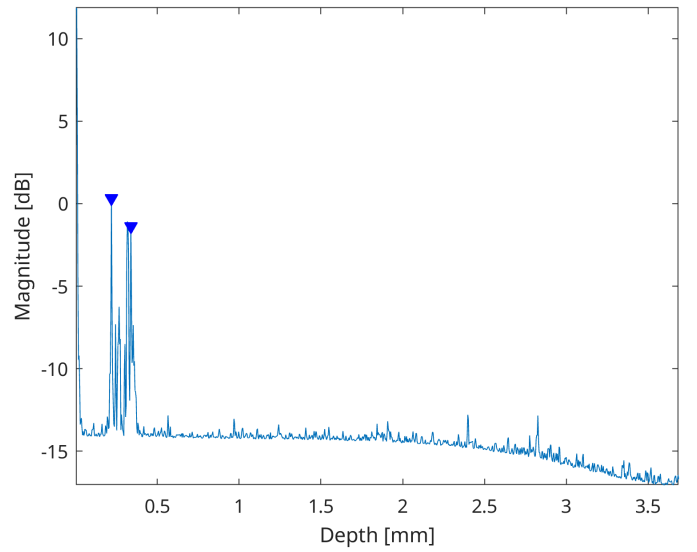


Fig. 8: The average magnitude of the Mscan1 data.

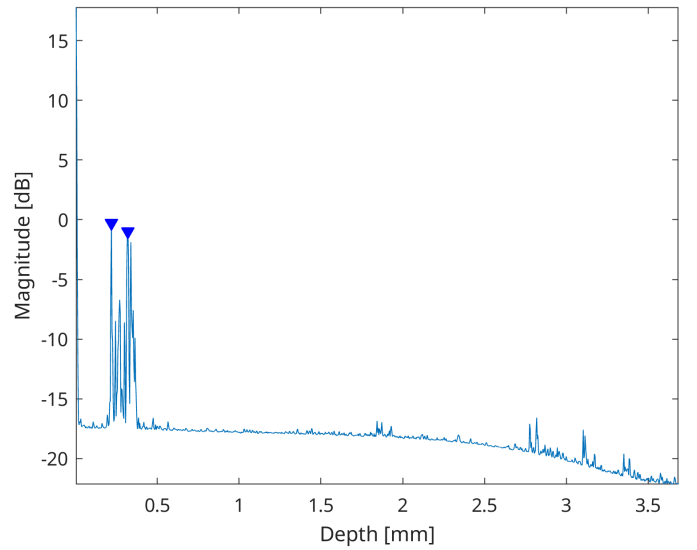


Fig. 9: The average magnitude of the Mscan40 data.

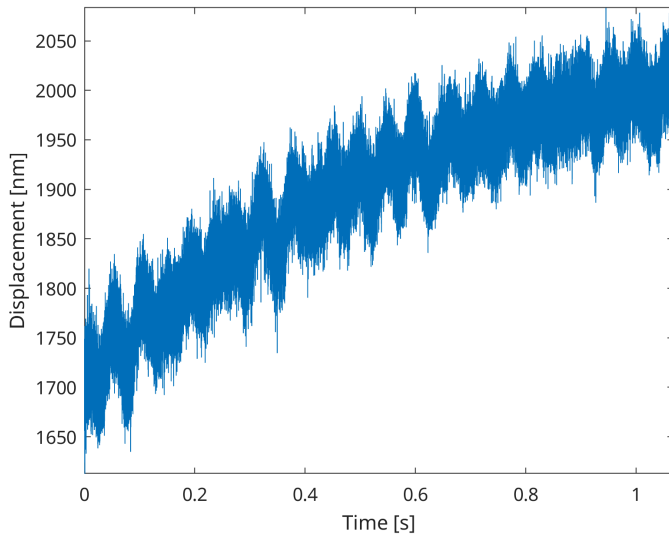


Fig. 10: Displacement of the Mscan1 data. A) the first A-scan of the Bscan data B) A-scan at the center of the Bscan data C) A-scan at the center of the Mscan1 data D) A-scan at the center of the Mscan40 data

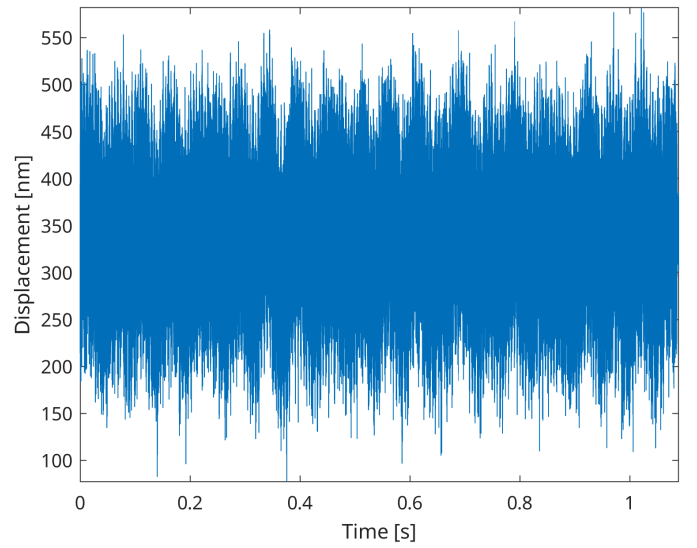


Fig. 12: Displacement of the Mscan40 data. A) the first A-scan of the Bscan data B) A-scan at the center of the Bscan data C) A-scan at the center of the Mscan1 data D) A-scan at the center of the Mscan40 data

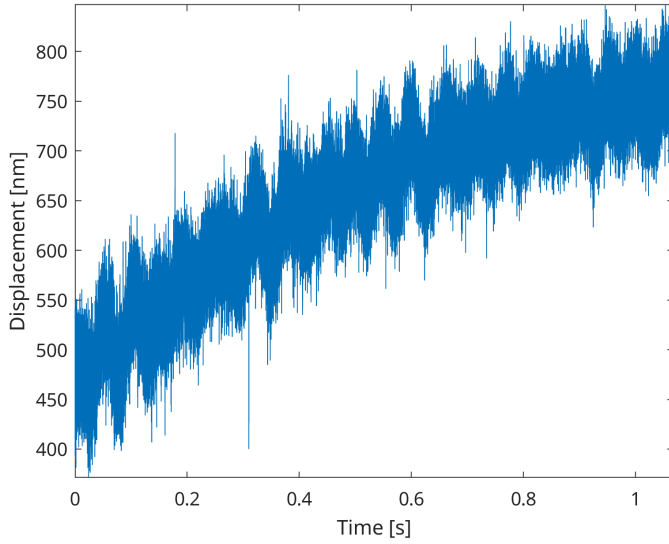


Fig. 11: Displacement of the Mscan1 data. A) the first A-scan of the Bscan data B) A-scan at the center of the Bscan data C) A-scan at the center of the Mscan1 data D) A-scan at the center of the Mscan40 data

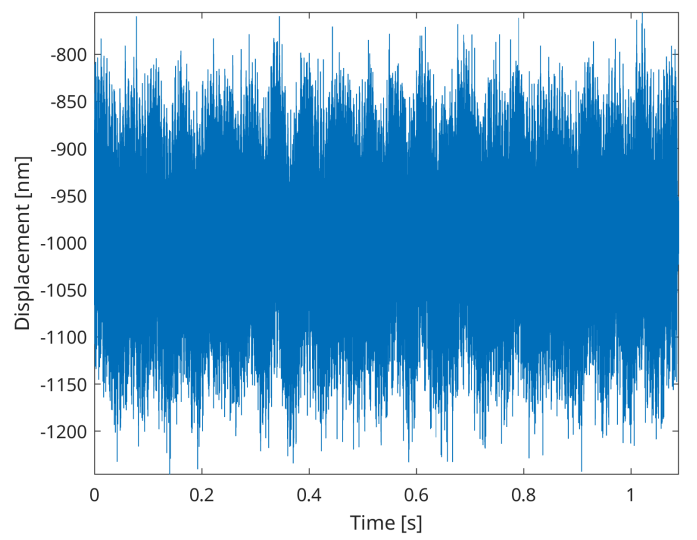


Fig. 13: Displacement of the Mscan40 data. A) the first A-scan of the Bscan data B) A-scan at the center of the Bscan data C) A-scan at the center of the Mscan1 data D) A-scan at the center of the Mscan40 data

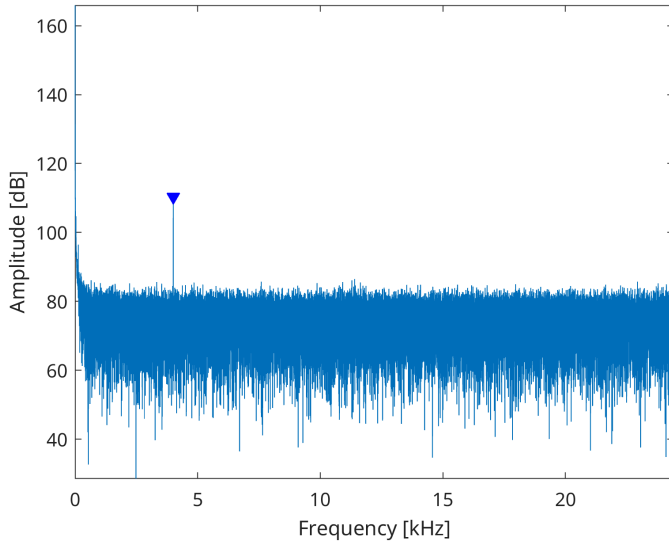


Fig. 14: Frequency of the Mscan1 data. A) the first A-scan of the Bscan data B) A-scan at the center of the Bscan data C) A-scan at the center of the Mscan1 data D) A-scan at the center of the Mscan40 data

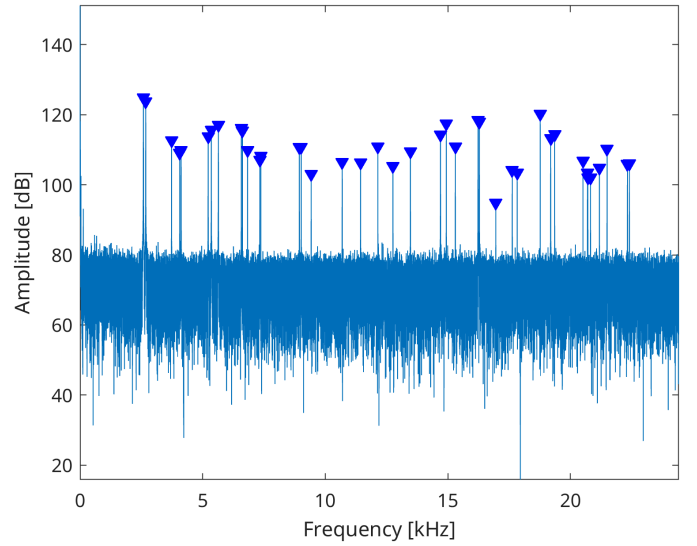


Fig. 16: Frequency of the Mscan40 data. A) the first A-scan of the Bscan data B) A-scan at the center of the Bscan data C) A-scan at the center of the Mscan1 data D) A-scan at the center of the Mscan40 data

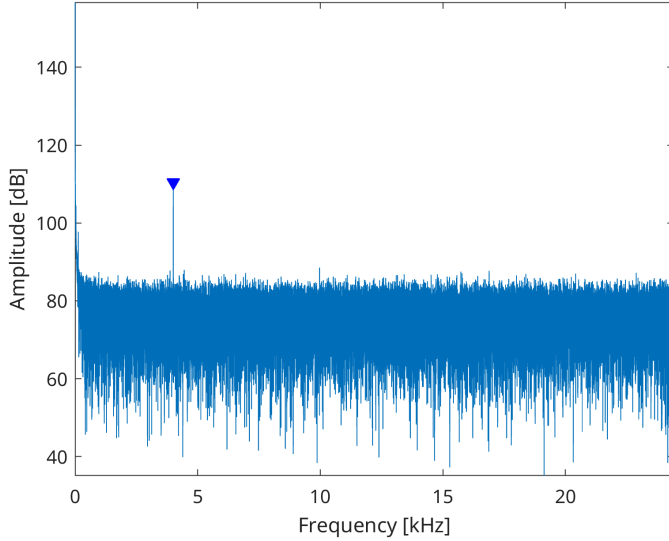


Fig. 15: Frequency of the Mscan1 data. A) the first A-scan of the Bscan data B) A-scan at the center of the Bscan data C) A-scan at the center of the Mscan1 data D) A-scan at the center of the Mscan40 data

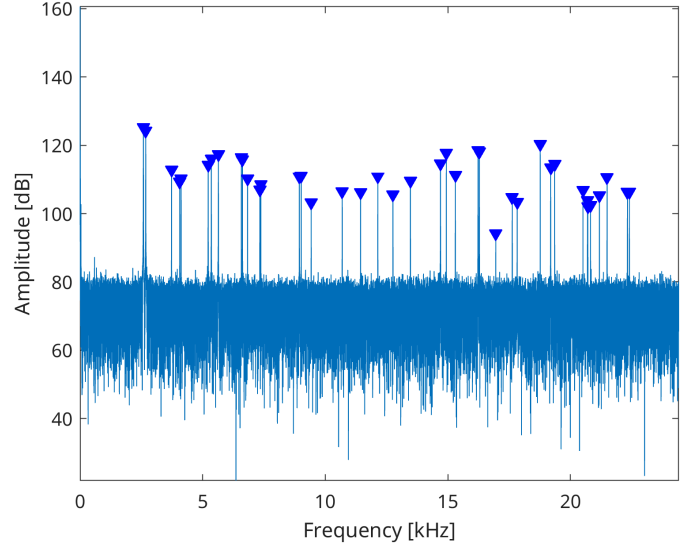


Fig. 17: Frequency of the Mscan40 data. A) the first A-scan of the Bscan data B) A-scan at the center of the Bscan data C) A-scan at the center of the Mscan1 data D) A-scan at the center of the Mscan40 data

#### IV. DISCUSSION

Comparing the B-scan images with and without deconvolution in Fig. 6, it seems that the deconvolution process does not significantly improve the image quality.

a) *Image Reconstruction Improvements*: Processed images significantly reduced background noise and mirror artifacts. Contrast enhancement using polynomial background fitting provided clear differentiation between layers, allowing precise identification of physical structures, such as tape layers.

b) *Displacement Measurement Accuracy*: The accuracy of sub-pixel displacement measurements was confirmed through spectral domain phase microscopy. Frequency domain analysis verified expected speaker output frequencies, supporting the system's sensitivity in measuring subtle displacements.

c) *Methodological Considerations:* The processing pipeline's efficiency was evaluated by timing computational steps. Background subtraction and deconvolution notably improved signal clarity, despite adding computational overhead. Future implementations could optimize processing time further by employing parallel processing techniques or GPU acceleration.

d) *Future Work:* Coupled with catheter, endoscopic, laparoscopic, or needle delivery devices, OCT promises to have a powerful impact on many medical applications ranging from the diagnosis of neoplasia, to enabling new minimally invasive surgical procedures.

## V. APPENDIX

### REFERENCES

- [1] J. A. Izatt and M. A. Choma, "Theory of Optical Coherence Tomography," *Optical Coherence Tomography: Technology and Applications*. Springer, Berlin, Heidelberg, pp. 47–72, 2008. doi: 10.1007/978-3-540-77550-8\_2.